

Phonon dynamics and chiral modes in the two-dimensional square-octagon lattice

Ravi Kiran^{1,*} and A. Taraphder^{1,†}

¹*Department of Physics, Indian Institute of Technology Kharagpur, Kharagpur 721302, West Bengal, India*

Chiral phonons, originally identified in two-dimensional hexagonal lattices and later extended to kagome, square, and other lattices, have been extensively studied as manifestations of broken inversion and time-reversal symmetries in vibrational dynamics. In this work, we investigate the vibrational dynamics of the two-dimensional square-octagon lattice using a spring-mass model with central-force interactions. The model incorporates mass contrast and variable coupling strengths among nearest, next-nearest, and third-nearest neighbors. From the dynamical matrix, we obtain the phonon dispersion relations and identify tunable phononic band gaps governed by both mass and spring-constant ratios. The angular dependence of phase and group velocities is analyzed to reveal the pronounced anisotropy inherent to this lattice geometry. We also examine the distinctive features of the square-octagon geometry, including flat-band anomalies in the density of states and anisotropic sound propagation induced by longer-range couplings. In addition, we explore the emergence of chiral phonons by introducing a time reversal symmetry-breaking term in the dynamical matrix, and to elucidate their optical signatures, we construct a minimal model to study infrared circular dichroism arising from chiral phonon modes.

I. INTRODUCTION

Phonons, first introduced in the 1930s [1], are fundamental to understanding the thermal, mechanical, and transport properties of crystalline solids. The field of lattice dynamics, which investigates these quantized collective excitations, has since become an essential branch of condensed matter physics. Chiral phonons proposed by Zhang et.al [2] and later experimentally observed [3–5] has changed our understanding of how atomic vibrations can interact with electronic and magnetic degrees of freedom and thus has attracted great interest in recent years[6–12]. These quantized lattice vibrations with circular polarization and non-zero angular momentum are distinguished from conventional linearly polarized phonons by their rotational character. The emergence of chiral phonons requires primarily the breaking of time-reversal and/or inversion symmetries. When these symmetries are broken simultaneously, truly chiral phonons can emerge with well-defined handedness[13–16].

Another interesting avenue is the study of acoustic and phononic metamaterials which has witnessed considerable theoretical advancement, particularly in computational methods ranging from simple spring-mass models to sophisticated first-principles calculations [17–22]. These are artificially designed mechanical structures for obtaining emergent functionalities such as vibration isolation and adaptive behaviour. Nikitenkova et.al. [23] investigated the dispersion properties of two-dimensional phonon crystals with hexagonal symmetry, uncovering distinctive acoustic and optical characteristics arising from lattice symmetry and interaction dynamics. Study by Kushwaha et.al. [24] on acoustic band structures of periodic elastic composites has revealed complete phononic band gaps, underscoring the

potential of phononic crystals for wave control and vibration suppression. Phononic crystals have also been extensively studied for its interesting physical properties [25–29] and engineering applications [30–33]. More recently with the birth of the field of electronic topological insulators, topology also found a new path back to classical systems [34–37].

The geometry and symmetry of the underlying lattice play a central role in determining the nature of phonon excitations. In hexagonal lattices, for instance, the threefold rotational symmetry at high-symmetry points gives rise to phonon eigenmodes carrying quantized pseudoangular momentum.[2, 3] Beyond hexagonal systems, chiral phonons have also been predicted in square lattices, where their existence requires explicit breaking of time-reversal symmetry[38]. In the kagome lattice, chiral phonons with pronounced circular polarization have been observed at high-symmetry points; unlike in the hexagonal case, all three sublattices there vibrate with the same handedness.[39] Triangular lattices have further been shown to host chiral phonons with nontrivial topological character, where the chirality remains robust against variations in sublattice mass and interlayer coupling, reflecting intrinsic topological protection.[40]

In this work we investigate the phonon properties of the square-octagon lattice within a classical spring-mass framework. This lattice, comprising of four atoms per unit cell and known for hosting multiple flat electronic bands and van Hove singularities (vHS) [41, 42], remains largely unexplored from the perspective of lattice vibrations. We calculate the phonon dispersion for various mass ratios and spring constants by incorporating interactions beyond the nearest neighbors, thereby capturing the influence of longer-range couplings on the vibrational spectrum, along with the corresponding density of states (DOS), mode profiles, and the angular dependence of both phase and group velocities. Furthermore, we examine the emergence of chiral phonons in this lattice when time-reversal symmetry (\mathcal{T}) is explicitly bro-

* ravieroy123@iitkgp.ac.in

† arghya@phy.iitkgp.ac.in

ken. A recent study [43] has done group theory analysis offering experimental benchmarks using circularly polarized Raman scattering for identifying crystalline chirality. To highlight the connection between phonon helicity and optical activity we also construct a minimal model to study infrared circular dichroism arising from chiral phonon modes.

The remainder of this paper is organized as follows. In Sec. II, we introduce the model and outline the theoretical framework. Section III presents and discusses the numerical results. Finally, Sec. IV summarizes the main findings and provides concluding remarks.

II. MODEL AND METHODOLOGY

A. Model and equations of motion

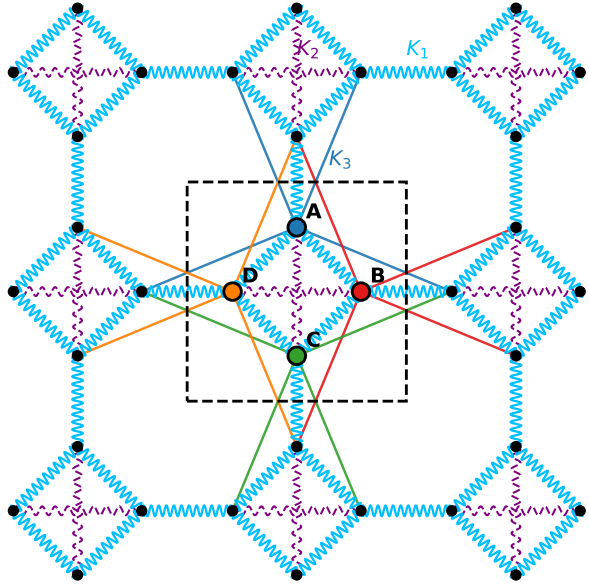


FIG. 1. Schematic representation of a 2D square-octagon lattice model, with a repeating unit cell outlined by a black dashed square containing four atomic sites. Nearest neighbor (NN) springs are shown as solid blue sinusoidal lines, next nearest neighbor (NNN) springs as dashed purple sinusoidal lines, and 3rd-NN connections as straight colored bonds extending from the central cell. The coupling constants K_1 , K_2 , and K_3 correspond to representative NN, NNN, and 3rd-NN interactions, respectively.

We consider oscillations of a square-octagon lattice (Fig. 1) with particles of masses m_α ($\alpha \in \{A, B, C, D\}$) positioned at the sites of the lattice. In equilibrium, the centers of the particles coincide with the lattice points, separated by a characteristic distance a . Each particle interacts with its nearest (NN), next-nearest(NNN), and 3rd-NN through springs of stiffness constants K_1 , K_2 ,

and K_3 , respectively. The unit cell contains four basis particles, labeled A , B , C , and D , whose centers define the fundamental motif of the lattice.

For a bond between sites (α, \mathbf{R}) and $(\beta, \mathbf{R} + \mathbf{R}')$, the bond vector is

$$\Delta = \mathbf{R}' + \tau_\beta - \tau_\alpha, \quad \hat{\Delta} = \frac{\Delta}{|\Delta|}, \quad (1)$$

where τ_α denotes the basis vector of particle α in the unit cell. The elastic energy stored in the bond is

$$E_{\alpha\beta}(\mathbf{R}) = \frac{1}{2} K_n [\hat{\Delta} \cdot (\mathbf{u}_\alpha(\mathbf{R}) - \mathbf{u}_\beta(\mathbf{R} + \mathbf{R}'))]^2, \quad (2)$$

where $K_n \in \{K_1, K_2, K_3\}$ depending upon whether the bond is NN, NNN, or 3rd-NN respectively. The displacement $\mathbf{u}_\alpha(\mathbf{R}, t)$ of atom α in cell \mathbf{R} at time t is written using the plane-wave ansatz

$$\mathbf{u}_\alpha(\mathbf{R}, t) = \tilde{\mathbf{u}}_\alpha \exp(i[\mathbf{k} \cdot (\mathbf{R} + \tau_\alpha) - \omega t]), \quad (3)$$

where $\tilde{\mathbf{u}}_\alpha \in \mathbb{C}^2$ is the polarization vector.

Taking derivatives of the elastic energy gives the forces as,

$$\frac{\partial E_{\alpha\beta}}{\partial \mathbf{u}_\alpha(\mathbf{R})} = K_n \hat{\Delta} \hat{\Delta}^\top (\mathbf{u}_\alpha(\mathbf{R}) - \mathbf{u}_\beta(\mathbf{R} + \mathbf{R}')), \quad (4)$$

$$\frac{\partial E_{\alpha\beta}}{\partial \mathbf{u}_\beta(\mathbf{R} + \mathbf{R}')} = -K_n \hat{\Delta} \hat{\Delta}^\top (\mathbf{u}_\alpha(\mathbf{R}) - \mathbf{u}_\beta(\mathbf{R} + \mathbf{R}')). \quad (5)$$

Thus, each central force contributes a projector $K_n \hat{\Delta} \hat{\Delta}^\top$ along the bond direction, and does not couple transverse components.

Substituting the ansatz, the displacement at $(\beta, \mathbf{R} + \mathbf{R}')$ is

$$\begin{aligned} \mathbf{u}_\beta(\mathbf{R} + \mathbf{R}', t) &= \tilde{\mathbf{u}}_\beta e^{i[\mathbf{k} \cdot (\mathbf{R} + \mathbf{R}' + \tau_\beta) - \omega t]} \\ &= \tilde{\mathbf{u}}_\beta e^{i\mathbf{k} \cdot \Delta} e^{i[\mathbf{k} \cdot (\mathbf{R} + \tau_\alpha) - \omega t]}. \end{aligned} \quad (6)$$

Each bond contributes a *phase factor* $e^{i\mathbf{k} \cdot \Delta}$ multiplying the neighbor amplitude. Newton's law, $m_\alpha \ddot{\mathbf{u}}_\alpha = \mathbf{f}_\alpha$, reduces to

$$m_\alpha \omega^2 \tilde{\mathbf{u}}_\alpha = \sum_{(\beta, \Delta) \in \mathcal{B}_\alpha} K_n \hat{\Delta} \hat{\Delta}^\top (\tilde{\mathbf{u}}_\alpha - \tilde{\mathbf{u}}_\beta e^{i\mathbf{k} \cdot \Delta}), \quad (7)$$

where \mathcal{B}_α is the set of all bonds (NN, NNN and 3rd-NN) incident on α .

Introducing mass-normalized amplitudes $\mathbf{e}_\alpha = \sqrt{m_\alpha} \tilde{\mathbf{u}}_\alpha$ we get,

$$\begin{aligned} \omega^2 \mathbf{e}_\alpha &= \sum_{(\beta, \Delta) \in \mathcal{B}_\alpha} \frac{K_n}{m_\alpha} \hat{\Delta} \hat{\Delta}^\top \mathbf{e}_\alpha \\ &\quad - \sum_{(\beta, \Delta) \in \mathcal{B}_\alpha} \frac{K_n}{\sqrt{m_\alpha m_\beta}} \hat{\Delta} \hat{\Delta}^\top e^{i\mathbf{k} \cdot \Delta} \mathbf{e}_\beta. \end{aligned} \quad (8)$$

Collecting $\{\mathbf{e}_\alpha\}$ into $E = (\mathbf{e}_A, \mathbf{e}_B, \mathbf{e}_C, \mathbf{e}_D)^\top$, we obtain the eigenvalue equation

$$\omega^2 E = \mathbf{D}(\mathbf{k}) E, \quad (9)$$

where $\mathbf{D}(\mathbf{k})$ is the dynamical matrix, of dimension 8×8 , Hermitian, and built from 2×2 blocks. The rules for constructing the blocks are,

$$\mathbf{D}_{\alpha\alpha} = \sum_{(\beta, \Delta) \in \mathcal{B}_\alpha} \frac{K_n}{m_\alpha} \hat{\Delta} \hat{\Delta}^\top, \quad (10)$$

$$\mathbf{D}_{\alpha\beta} = - \sum_{\Delta} \frac{K_n}{\sqrt{m_\alpha m_\beta}} \hat{\Delta} \hat{\Delta}^\top e^{i\mathbf{k}\cdot\Delta}, \quad \alpha \neq \beta, \quad (11)$$

$$\mathbf{D}_{\beta\alpha} = \mathbf{D}_{\alpha\beta}^\dagger. \quad (12)$$

Equivalently, defining the real-space force constants $\mathbf{C}_{\alpha\beta}(\mathbf{R}')$ for bonds connecting $(\alpha, \mathbf{0})$ to (β, \mathbf{R}') ,

$$\mathbf{C}_{\alpha\beta}(\mathbf{R}') = \begin{cases} \sum_{(\beta, \Delta)} K_n \hat{\Delta} \hat{\Delta}^\top, & \alpha = \beta, \\ -K_n \hat{\Delta} \hat{\Delta}^\top, & \text{if } \Delta = \mathbf{R}' + \tau_\beta - \tau_\alpha, \\ \mathbf{0}, & \text{otherwise,} \end{cases} \quad (13)$$

the dynamical matrix follows from the lattice Fourier transform

$$\mathbf{D}_{\alpha\beta}(\mathbf{k}) = \frac{1}{\sqrt{m_\alpha m_\beta}} \sum_{\mathbf{R}'} \mathbf{C}_{\alpha\beta}(\mathbf{R}') e^{i\mathbf{k}\cdot(\mathbf{R}' + \tau_\beta - \tau_\alpha)}. \quad (14)$$

The 2×2 matrix $\mathbf{P}(\Delta) = \hat{\Delta} \hat{\Delta}^\top$ is the *projection matrix* onto the bond direction. For any vector \mathbf{v} , we have $\mathbf{P}(\Delta)\mathbf{v} = (\hat{\Delta} \cdot \mathbf{v})\hat{\Delta}$. Thus, $\mathbf{P}(\Delta)$ extracts the longitudinal component of \mathbf{v} parallel to the bond, making explicit that central springs resist only relative motion along Δ . For later use we also introduce four auxiliary 2×2 matrices: $\mathbf{P}_1 = \frac{1}{2} \begin{bmatrix} 1 & -1 \\ -1 & 1 \end{bmatrix}$, $\mathbf{P}_2 = \frac{1}{2} \begin{bmatrix} 1 & 1 \\ 1 & 1 \end{bmatrix}$, $\mathbf{X} = \begin{bmatrix} 1 & 0 \\ 0 & 0 \end{bmatrix}$, and $\mathbf{Y} = \begin{bmatrix} 0 & 0 \\ 0 & 1 \end{bmatrix}$. $\mathbf{D}(\mathbf{k})$ is a 4×4 block matrix with the form,

$$\mathbf{D}(\mathbf{k}) = \begin{pmatrix} \mathbf{D}_{11} & \mathbf{D}_{12} & \mathbf{D}_{13} & \mathbf{D}_{14} \\ \mathbf{D}_{21} & \mathbf{D}_{22} & \mathbf{D}_{23} & \mathbf{D}_{24} \\ \mathbf{D}_{31} & \mathbf{D}_{32} & \mathbf{D}_{33} & \mathbf{D}_{34} \\ \mathbf{D}_{41} & \mathbf{D}_{42} & \mathbf{D}_{43} & \mathbf{D}_{44} \end{pmatrix}, \quad (15)$$

The phonon frequencies follow from the equation, $\det[\omega^2(\mathbf{k}) \mathbf{I}_8 - \mathbf{D}(\mathbf{k})] = 0$. The detailed form of the matrix entries is shown in Appendix A.

B. Time-reversal-symmetry breaking in the phonon dynamical matrix

The dynamical matrix given in Eqn. 15 preserves time-reversal symmetry and to induce phonon chirality, we introduce a weak time reversal symmetry breaking term. Previous studies have achieved this by adding a \mathcal{T} -breaking perturbation to the Hamiltonian [38, 44, 45] and the origin of such perturbations could

be from the Lorentz force[45], Raman-type spin-phonon interaction[44], or Coriolis force[46].

We implement this by modifying each bond matrix as

$$\Phi(\mathbf{r}_{ij}) = \Phi_0(\mathbf{r}_{ij}) + \Phi_{\text{chiral}}(\mathbf{r}_{ij}) \quad (16)$$

$$\Phi(\mathbf{r}_{ij}) = \Phi_0(\mathbf{r}_{ij}) + ig \frac{r_{ij,x}}{|\mathbf{r}_{ij}|} S_2, \quad (17)$$

where $S_2 = \begin{pmatrix} 0 & -1 \\ 1 & 0 \end{pmatrix}$, g is a dimensionless gyroscopic coupling parameter and the geometric factor $\frac{r_{ij,x}}{|\mathbf{r}_{ij}|}$ signifies the directional dependence of the gyroscopic coupling between sites i and j . In reciprocal space, the dynamical matrix becomes

$$D(\mathbf{k}) = D_0(\mathbf{k}) + ig G(\mathbf{k}),$$

where D_0 is the usual real symmetric matrix obtained from central springs, and $G(\mathbf{k})$ is an antisymmetric matrix that mixes the in-plane x and y components. Because $D(\mathbf{k})$ is now complex Hermitian, its eigenvectors are generally complex, corresponding to elliptically or circularly polarized atomic motions. At high-symmetry points where the two in-plane polarizations are degenerate, the antisymmetric term acts within the $\{x, y\}$ subspace as

$$D_{\text{eff}} = \begin{pmatrix} \omega_0^2 & -ig_{\text{eff}} \\ ig_{\text{eff}} & \omega_0^2 \end{pmatrix},$$

leading to split eigenfrequencies $\omega_\pm^2 = \omega_0^2 \pm g_{\text{eff}}$, and eigenvectors $\mathbf{e}_\pm = \frac{1}{\sqrt{2}}(1, \pm i)^\top$, which represent circularly polarized atomic motions with opposite angular momentum L_z . This splitting converts originally degenerate linear modes into chiral phonons with well-defined helicity. The resulting Hermitian dynamical matrix $D(\mathbf{k})$ is diagonalized to obtain frequencies $\omega_\lambda(\mathbf{k})$ and eigenmodes $\mathbf{e}_{\mathbf{k}\lambda}$. The phonon angular momentum for each mode is then evaluated as [2, 47]

$$L_z(\mathbf{k}, \lambda) = \sum_\alpha m_\alpha \text{Im}[e_{\alpha x}^*(\mathbf{k}, \lambda) e_{\alpha y}(\mathbf{k}, \lambda)], \quad (18)$$

which serves as a quantitative measure of phonon chirality and determines the sign of the Raman circular dichroism.

III. RESULTS

A. Phonon band structure and DOS

In this section, we present representative phonon spectra obtained for different mass ratios and spring constants. The model includes NN, NNN, and 3rd-NN interactions characterized by coupling strengths K_1, K_2 ,

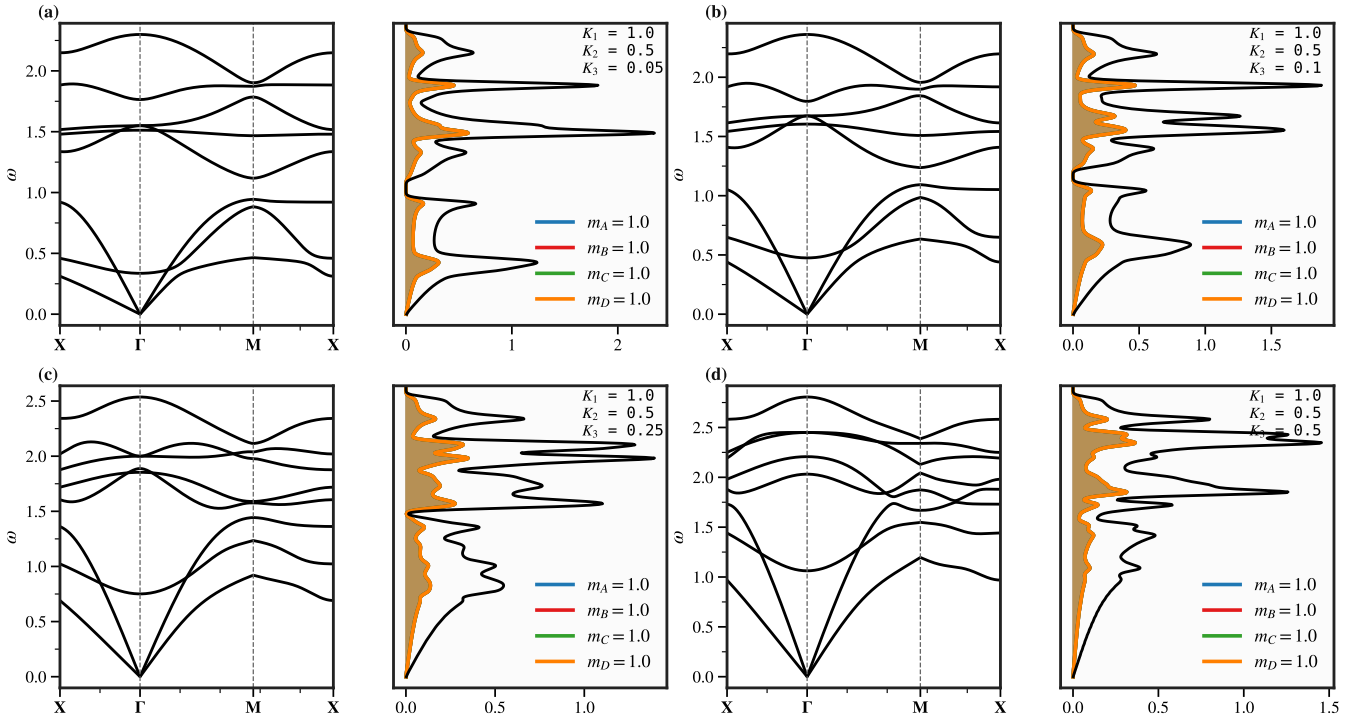


FIG. 2. Phonon dispersions along the $X-\Gamma-M-X$ path and the corresponding atom-projected density of states for the uniform-mass case ($m_\alpha = 1$) with fixed NNN coupling $K_2 = 0.5$ and increasing third-neighbor coupling, (a) $K_3 = 0.05$, (b) $K_3 = 0.1$, (c) $K_3 = 0.25$, and (d) $K_3 = 0.5$. The color shading in the DOS indicates the relative contributions of individual sublattices to each vibrational mode.

and K_3 , respectively. The inclusion of the 3rd-NN term is essential, as several phonon modes (namely at $q = 0$ and $q = \sqrt{2}$) remain dispersionless when $K_3 = 0$. The corresponding results for $K_3 = 0$ are discussed separately in Appendix B.

We start with the simple case of uniform masses ($m_\alpha = 1.0$) and show the results by varying K_3 in Fig. 2. Even for small K_3 as shown in Fig. 2(a), the frozen mode at $q = 0$ is lifted and a vHS appears at the M point, while the higher-frequency frozen mode at $q = \sqrt{2}$ persists, though with weak dispersion. A clear acoustic-optical separation remains near $\omega \approx 1.0$, and the identical site masses yield equal contributions in the projected DOS (PDOS). Increasing K_3 reduces the gap and enhances the dispersion of the frozen mode as shown in Fig. 2(b) and Fig. 2(c), and at stronger coupling this trend continues until the gap vanishes (Fig. 2(d)) due to significant hybridization between acoustic and optical modes.

We next examine the effect of mass variations on the phonon bands and DOS. Figure 3(a) shows the case of weak 3rd-NN coupling with small mass contrast. As shown in Fig. 2(a), for the uniform-mass lattice, the degeneracy of the phonon branches at the M point originates from the equivalence of the atomic environments. Introducing a finite mass contrast lifts this degeneracy by effectively reducing the lattice symmetry. The impact of mass contrast is evident in the projected density of states (PDOS), where the resulting frequency splitting

reflects the differing responses of the heavier and lighter atoms. In particular, the lighter sublattice contributes more prominently to the higher-frequency modes.

Increasing K_3 to moderate values (Fig. 3(b)) introduces competition between mass contrast and long-range interactions, as the additional stiffness couples the sublattices and delocalizes the modes which can be seen in the resulting hybridization in the PDOS.

Fig. 3(c) illustrates the extreme case of very large mass contrast. In this limit, the heavier atoms behave as slow, weakly coupled oscillators, effectively decoupling subsets of degrees of freedom and producing pronounced van Hove peaks. Multiple phonon gaps emerge, and the PDOS becomes strongly segregated, lighter atoms contribute broad, high-frequency features, while heavier atoms yield narrow, low-frequency modes. Such strong mass contrast can provide a route to phonon band engineering, enabling flat bands and low-frequency localized modes, and can substantially suppress thermal transport by reducing group velocities and enhancing scattering.

Finally, Fig. 3(d) shows the effect of introducing a light impurity or defect into the lattice. The impurity contributes high-frequency spectral weight well above the main band manifold, producing a sharp DOS peak dominated by the light sublattice. These resonant modes strongly scatter heat-carrying phonons, offering an effective mechanism to reduce thermal conductivity through resonant phonon scattering. They are also spectroscop-

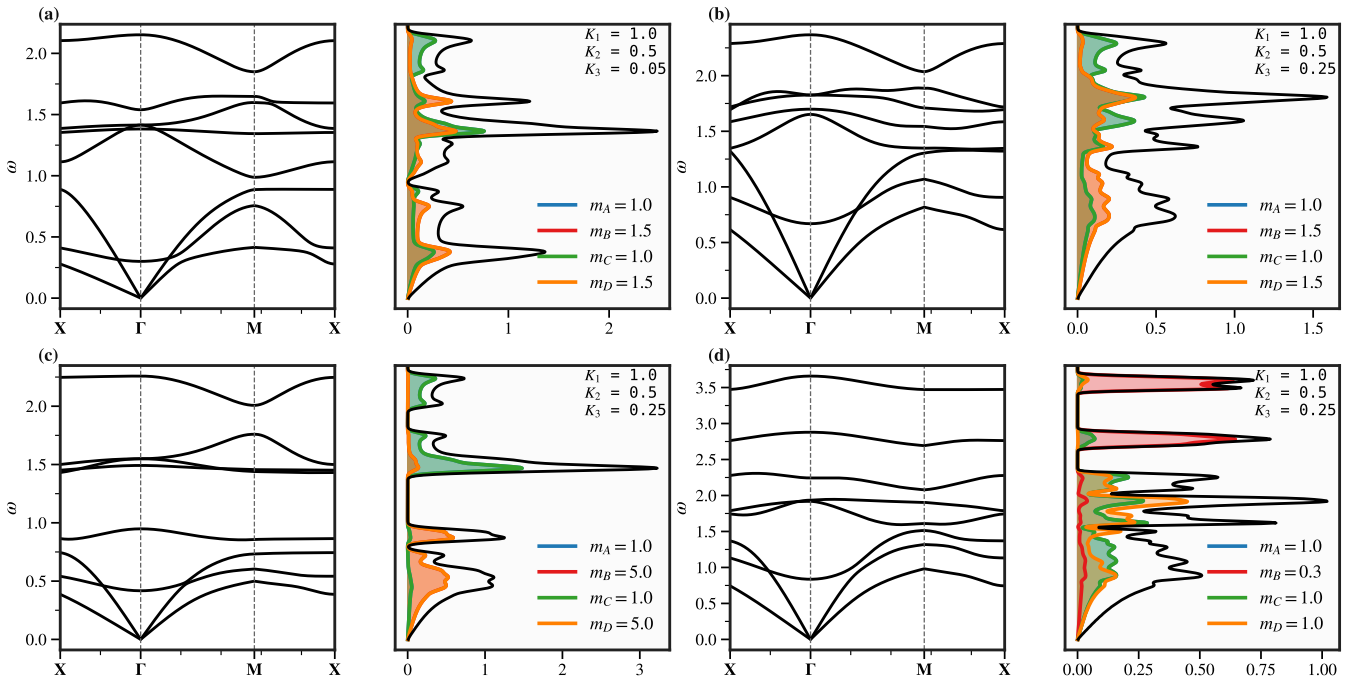


FIG. 3. Phonon dispersions along the $X-\Gamma-M-X$ path and the corresponding atom-projected density of states for the square-octagon lattice with fixed couplings $K_1 = 1.0$ and $K_2 = 0.5$, and varying 3rd-NN coupling K_3 . (a) Weak long-range coupling with small mass contrast ($m_A = m_C = 1.0$, $m_B = m_D = 1.5$, $K_3 = 0.05$); (b) moderate coupling with the same mass configuration ($K_3 = 0.25$); (c) large mass contrast ($m_A = m_C = 1.0$, $m_B = m_D = 5.0$, $K_3 = 0.25$); and (d) a light impurity on the B sublattice ($m_B = 0.3$, others unity, $K_3 = 0.25$). The color shading in the DOS indicates the relative contributions of individual sublattices to each vibrational mode.

ically distinct, with signatures in Raman and infrared measurements, since the vibrational amplitude is concentrated on a small subset of atoms.

B. Phonon Modes

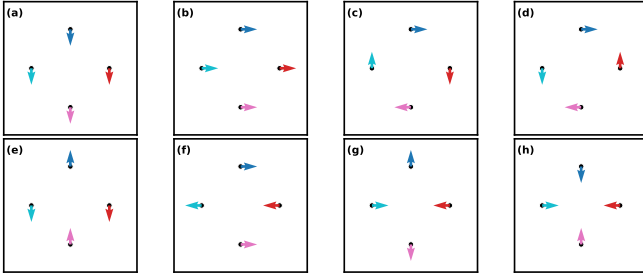


FIG. 4. Representative phonon eigenmodes of the square-octagon lattice at high-symmetry point Γ . (a) and (b) correspond to acoustic-like translations, with all atoms moving in phase along orthogonal directions. (c), (d), (e), and (f) represent optical shear or stretching distortions where sublattices move out of phase and (g) and (h) show breathing-type modes. Together these eight patterns illustrate the characteristic vibrational motifs of the lattice.

In the square-octagon lattice, the phonon eigenmodes

at high-symmetry points Γ can be grouped into a few characteristic motifs. Two modes as shown in Fig. 4(a) and Fig. 4(b) correspond to acoustic-like translations in which all atoms move nearly in phase along orthogonal directions, analogous to transverse and longitudinal acoustic modes in simpler lattices. Modes shown in Fig. 4 (c), (d), (e), and (f) are optical in character as sublattices move out of phase with one another, producing shear or stretching like distortions along the principal lattice directions. Two further optical modes (Fig. 4(g) and Fig. 4(h)) exhibit breathing-type motion, where atoms are displaced radially inward or outward, leading to bond-length modulation without net translation of the unit cell.

At the X and M points, the phonon eigenmodes can be interpreted as linear combinations of the displacement motifs identified at Γ . At X (Fig. 5(a-d)), the modes are more shear and stretching like distortions align with the reciprocal lattice vector. At M as shown in Fig. 5(e-h), the motifs are hybridized and rotated, combining features of shear and breathing modes along diagonal directions. Although the symmetry is reduced compared to Γ , the underlying character of the eigenmodes remains consistent with the translational, shear, and breathing archetypes.

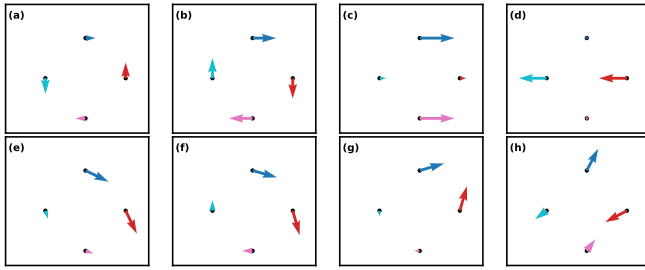


FIG. 5. Phonon eigenmodes of the square-octagon lattice at high-symmetry points X (a-d) and M (e-h). At X , the modes are predominantly shear and stretching type. At M , the modes appear as rotated or hybridized versions of the Γ -point motifs, combining shear and breathing distortions along diagonal directions.

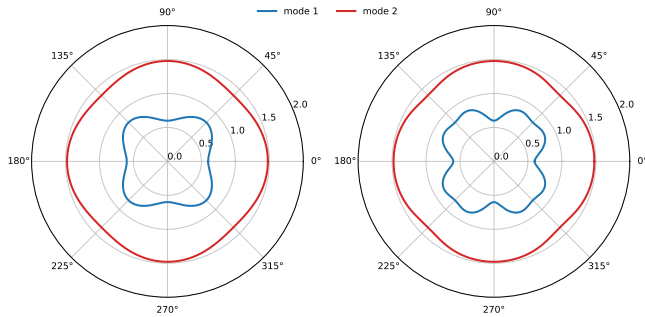


FIG. 6. (a) Phase and (b) group velocity polar plots of the two acoustic branches at $q = 0.01$ for the square-octagon lattice with $m = 1$, $K_1 = 1.0$, $K_2 = 0.5$, and $K_3 = 0.25$. The faster (red) mode is longitudinal-like while the slower (blue) mode is transverse-like. Both quantities exhibit fourfold anisotropy, with the group velocities showing sharper angular variations due to finite- q dispersion curvature.

C. Phase and group velocities

To characterize the low-momentum acoustic response of the square-octagon lattice, we calculated the phase and group velocities of the two acoustic branches at $q = 0.01$ for equal atomic masses ($m_\alpha = 1$) and spring constants $K_1 = 1.0$, $K_2 = 0.5$, and $K_3 = 0.25$ (see Fig. 2(c) for the corresponding phonon bands). These parameters are representative, as the qualitative behavior remains similar across a wide range of values. Figures 6(a) and 6(b) display the polar plots of the phase and group velocities, respectively. Both exhibit clear fourfold anisotropy consistent with the lattice symmetry, with mode 1 showing longitudinal-like character and mode 2 transverse-like character. The angular modulation arises from the combined effects of nearest-neighbor (K_1) and longer-range couplings (K_2 and K_3), which enhance stiffness along the diagonals and generate higher-order harmonics in the velocity profiles. Compared with the phase velocity, the group velocity shows stronger angular variations, reflecting the pronounced influence of anisotropy even at small

but finite q .

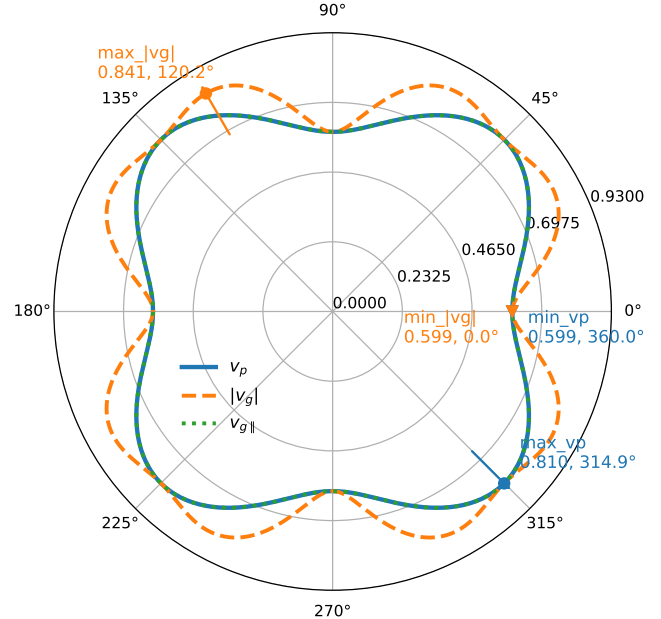


FIG. 7. Comparison of the phase velocity v_p , the magnitude of the group velocity $|\mathbf{v}_g|$, and its projection along the propagation direction $v_{g\parallel} = \hat{\mathbf{q}} \cdot \mathbf{v}_g$ for mode 1 at $q = 0.01$. While v_p and $v_{g\parallel}$ nearly coincide and display a fourfold modulation set by the lattice symmetry, $|\mathbf{v}_g|$ exhibits sharper angular variations. The annotated extrema indicate the directions of maximum and minimum velocities, highlighting the anisotropic character of acoustic propagation.

We focus a little more on the anisotropy for mode 1 and look at it more closely. Fig. 7 compares the phase velocity $v_p(\theta) = \omega(\mathbf{q})/|\mathbf{q}|$, the magnitude of the group velocity $|\mathbf{v}_g|$, and its projection along the propagation direction, $v_{g\parallel}(\theta) = \hat{\mathbf{q}} \cdot \mathbf{v}_g$, where $\hat{\mathbf{q}} = \mathbf{q}/|\mathbf{q}|$. For the isotropic system, in the long wavelength limit we expect and studies have shown [23] that the phase velocities do not depend on the angle and it coincides with group velocity. For the present case, in the long wavelength limit, v_p and $v_{g\parallel}$ coincides, consistent with the linear dispersion near Γ and $|\mathbf{v}_g|$ exhibits stronger angular modulation, with extrema shifted relative to those of v_p .

To further examine the acoustic response, we see the evolution of the polar plots of $v_p(\theta)$, $|\mathbf{v}_g(\theta)|$, and $v_{g\parallel}(\theta)$ with increasing momentum, as shown in Fig. 8. At small q , v_p and $v_{g\parallel}$ coincide. At intermediate momentum ($q = 0.2$, Fig. 8(a)), deviations between $|\mathbf{v}_g|$ and $v_{g\parallel}$ become evident, indicating that the energy flow is no longer strictly collinear with the propagation vector. Near the Brillouin-zone boundary ($q = 0.5$, Fig. 8(b)), this discrepancy is most pronounced and $|\mathbf{v}_g|$ exhibits sharp angular modulations, while v_p maintains a smoother fourfold character.

To quantify the angular anisotropy of the phase velocity and to verify that it is not an artifact of the chosen q , we expanded $v_p(\theta)$ in a Fourier series and extracted the

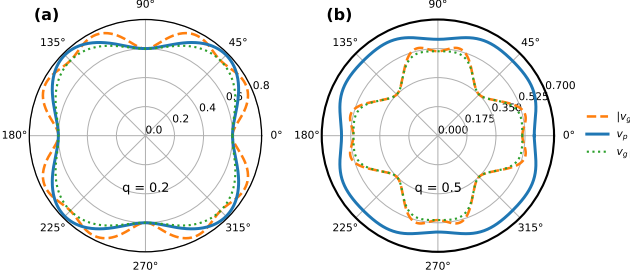


FIG. 8. Polar plots of the phase velocity v_p , group velocity magnitude $|v_g|$, and the parallel group velocity $v_{g,||}$ for mode 1 at representative wavevectors. Here q is expressed in units of $|\mathbf{b}_1|$. (a) At $q = 0.2$, deviations between $|v_g|$ and $v_{g,||}$ become more pronounced, indicating that the group velocity tilts away from the wavevector. (b) At $q = 0.5$, $|v_g|$ exhibits strong fourfold modulation, whereas v_p retains a smoother angular dependence.

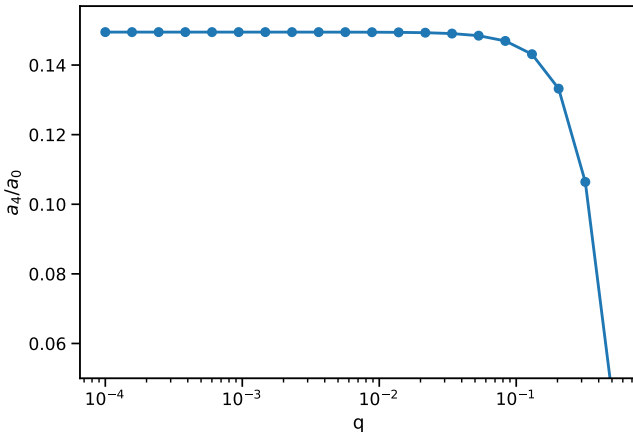


FIG. 9. Fourfold anisotropy ratio a_4/a_0 of the phase velocity as a function of q , expressed in units of $|\mathbf{b}_1|$. The ratio remains nearly constant at ~ 0.15 for $q \ll |\mathbf{b}_1|$, showing that the long-wavelength response is intrinsically anisotropic. At larger q , a_4/a_0 decreases rapidly, reflecting reduced angular contrast near the Brillouin-zone boundary.

ratio a_4/a_0 , which measures the relative weight of the fourfold harmonic compared to the isotropic average (see Appendix C for details). Figure 9 shows that this ratio saturates to a nearly constant value of approximately 0.15 in the long-wavelength limit ($q \ll |\mathbf{b}_1|$), indicating that the anisotropy persists even as $q \rightarrow 0$. As the momentum increases, the ratio decreases rapidly, reflecting the flattening of the dispersion near the Brillouin zone boundary. This suggests a strong indication that the low- q anisotropy originates from the inherent lattice symmetry, whereas at higher q the detailed band structure governs the velocity profile.

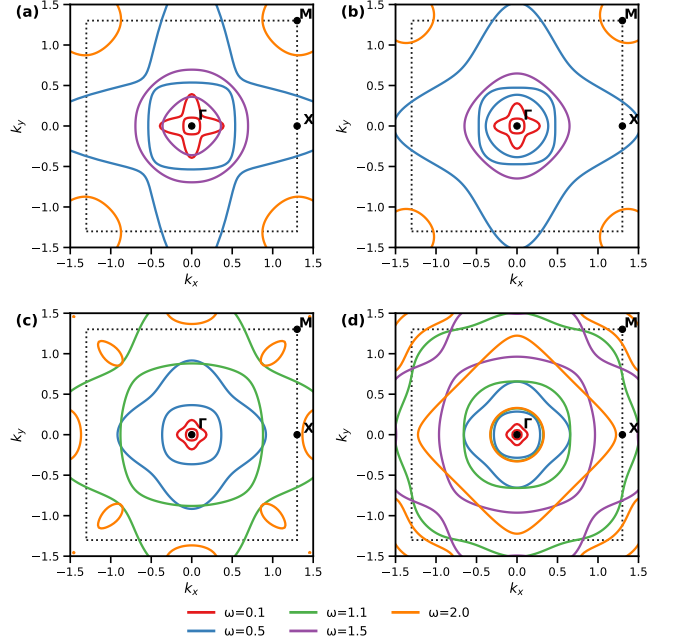


FIG. 10. Iso-frequency contours of the square-octagon lattice with uniform masses ($m_\alpha = 1$), NN coupling $K_1 = 1.0$, NNN coupling $K_2 = 0.5$, and varying 3rd-NN coupling K_3 . (a) $K_3 = 0.05$; (b) $K_3 = 0.1$; (c) $K_3 = 0.25$; (d) $K_3 = 0.5$. The dotted square is the first Brillouin zone.

D. Iso-frequency surfaces

Iso-frequency surfaces represent constant-frequency contours in reciprocal space and provide a direct visualization of phonon propagation characteristics and anisotropy which offers insights into vibrational transport and scattering processes in crystalline materials. In this section we present the isofrequency surfaces for the phonon bands in Sec. III A, focusing first on the uniform-mass case ($m_\alpha = 1.0$) with $K_1 = 0.5$ and varying K_3 . The illustrative case for $K_3 = 0$ is discussed separately in Appendix D.

We begin with the case of a weak long-range interaction, $K_3 = 0.05$, and uniform atomic masses ($m_\alpha = 1.0$). As discussed earlier, introducing a finite 3rd-NN coupling removes the frozen modes present in the case of $K_3 = 0$ (Appendix D, Fig. 18), leading to two distinct acoustic branches near the Brillouin zone center, as shown in Fig. 2. These two low-energy modes, however, display different anisotropic characteristics. As shown in Fig. 10(a), for $\omega = 0.1$, the longitudinal mode exhibits an almost circular iso-frequency contour around the Γ point, while the transverse mode forms a four-lobed structure reflecting the underlying fourfold lattice symmetry. No iso-frequency contour appears within the phonon gap ($\omega = 1.1$). The nearly flat band and corresponding VHS near $\omega = 1.5$, visible in the DOS, give rise to a nearly isotropic contour for $K_3 = 0.05$, which evolves into a distinctly fourfold lobe pattern when K_3 is increased to 0.1

(Fig. 10(b)). Upon further increasing the long-range coupling to $K_3 = 0.25$ (Fig. 10(c)), additional iso-frequency contours appear around $\omega = 1.1$, corresponding to modes that were previously gapped. At even stronger coupling, $K_3 = 0.5$, the phonon branches hybridize significantly, resulting in multiple overlapping iso-frequency surfaces.

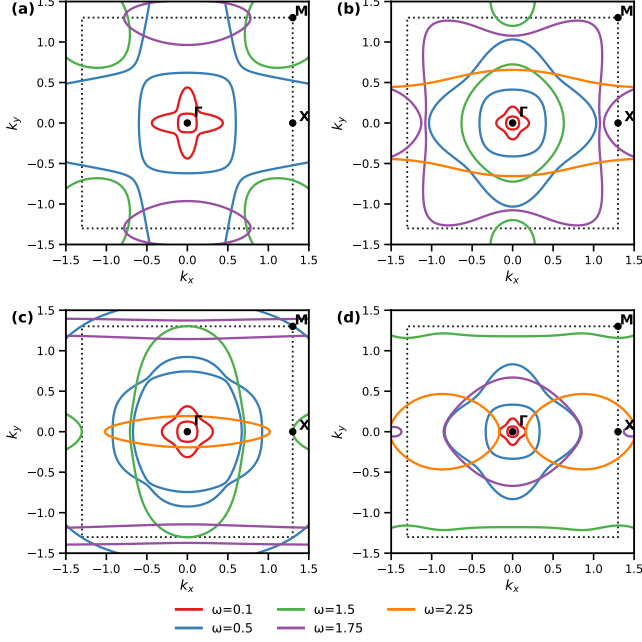


FIG. 11. Iso-frequency contours of the square-octagon lattice with $K_1 = 1.0$, $K_2 = 0.5$, and finite 3rd-NN coupling K_3 , for different sublattice mass distributions. (a) $m_A = m_C = 1.0$, $m_B = m_D = 1.5$, $K_3 = 0.05$; (b) $m_A = m_C = 1.0$, $m_B = m_D = 1.5$, $K_3 = 0.25$; (c) $m_A = m_C = 1.0$, $m_B = m_D = 5.0$, $K_3 = 0.25$; (d) $m_A = m_C = m_D = 1.0$, $m_B = 0.3$, $K_3 = 0.25$.

Next, in Fig. 11 we show the effect of variations in sublattice masses on the iso-frequency contours. For all mass contrasts, we observe similar features as in the uniform-mass case for low frequencies ($\omega = 0.1$ and $\omega = 0.5$), with circular contours centered at Γ and closed loops near the Brillouin zone boundaries, indicating the nonmonotonic dispersion. The more intriguing behavior emerges at higher frequencies. For example, the $\omega = 1.75$ contour initially lies along the zone boundary for small K_3 , signifying band-edge modes with vanishing group velocity, however, as K_3 increases, this contour shifts inward, revealing the onset of propagating phonon states at the same frequency. At still larger K_3 , the contour becomes elongated and nearly parallel to the k_x axis, reflecting strong anisotropy and quasi-one-dimensional phonon transport.

E. Chiral Phonons

We break time-reversal symmetry in the square-octagon lattice following the procedure outlined in

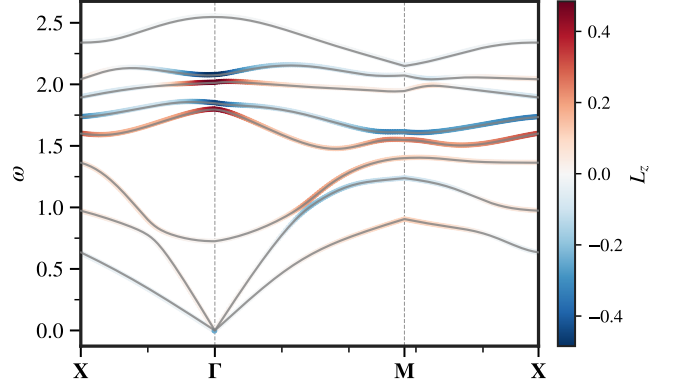


FIG. 12. Phonon band structure in the presence of a finite time-reversal symmetry breaking term $g = 0.1$ for a system with masses $(1.0, 1.0, 1.0, 1.0)$ and spring constants $K_1 = 1.0$, $K_2 = 0.5$, and $K_3 = 0.25$. The color scale represents the phonon angular momentum $L_z(\mathbf{k})$. Finite L_z values around the Γ point indicate the emergence of chiral phonon modes.

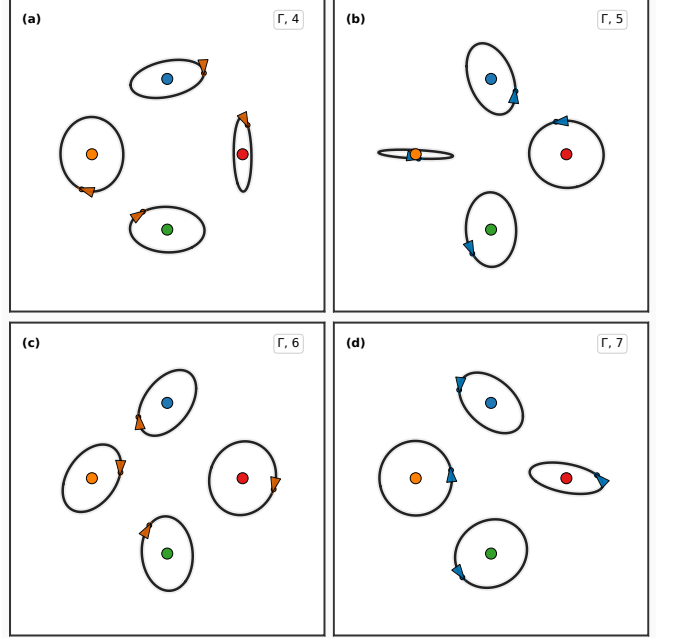


FIG. 13. Phonon eigenmodes at the Γ point for bands 4–7, shown for a system with uniform masses $m_\alpha = 1.0$ and spring constants $K_1 = 1.0$, $K_2 = 0.5$, and $K_3 = 0.25$, in the presence of a \mathcal{T} -breaking term $g = 0.1$. The orange and blue arrows denote counterclockwise and clockwise rotations, respectively, illustrating the alternating helicities of the chiral phonon modes.

Sec. II B. In Fig. 12 we show the resulting phonon band structure for a system with uniform masses ($m_\alpha = 1.0$) and spring constants $K_1 = 1.0$, $K_2 = 0.5$, and $K_3 = 0.25$, in the presence of a finite symmetry-breaking term ($g = 0.1$). For these parameters, the bands are degenerate at high-symmetry points Γ and M (see Fig. 2(c)), and the introduction of a nonzero g lifts these degen-

eracies. The resulting splittings of previously degenerate branches at Γ and M signify the onset of finite phonon angular momentum. In Fig. 13, we display the corresponding phonon polarizations for modes at Γ for bands 4–7. The direction and handedness of the elliptical trajectories reveal the intrinsic circular polarization of the phonon modes, with alternating helicities between adjacent bands. Although the lattice possesses overall C_4 symmetry, the inclusion of third-neighbor couplings shifts the local rotation centers away from atomic sites, causing the vibrational trajectories of individual sublattices to deviate from perfect circular motion.

In Fig. 14(a), we present the phonon band structure for a lattice with masses $(1.0, 1.5, 1.0, 1.5)$ and spring constants $K_1 = 1.0$, $K_2 = 0.5$, and $K_3 = 0.25$, in the presence of a time-reversal-symmetry-breaking term $g = 0.1$. The corresponding spectrum for $g = 0$ is shown in Fig. 3(b). Similar to the uniform-mass case, the inclusion of a finite g lifts the degeneracies at high-symmetry points, leading to phonon modes with opposite angular momenta at the Γ point. Figures 14(b) and 14(c) show the phonon polarization ellipses at Γ for bands 6 and 7, respectively. For this configuration, the angular momenta of bands 4 and 5 are opposite in sign but small in magnitude. Interestingly, as shown in Fig. 15, reversing the mass sequence to $(1.5, 1.0, 1.5, 1.0)$ significantly increases the contributions of bands 4 and 5 to the total phonon angular momentum.

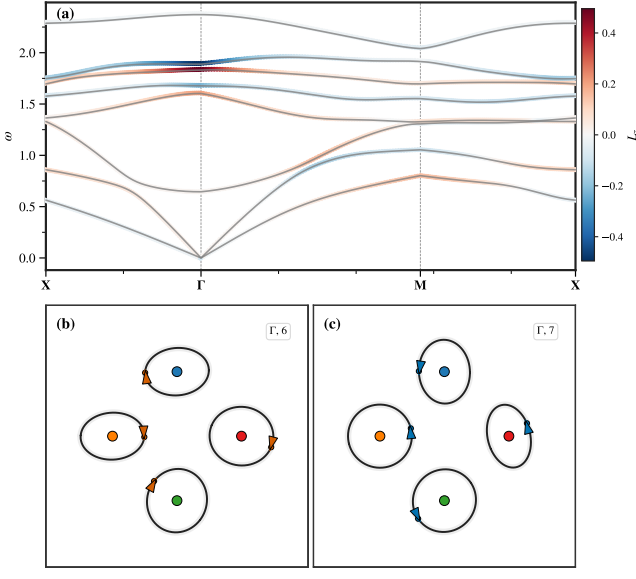


FIG. 14. Phonon band structure and phonon eigenmodes for the square-octagon lattice with masses $(1.0, 1.5, 1.0, 1.5)$, $K_1 = 1.0$, $K_2 = 0.5$, and $K_3 = 0.25$. (a) Phonon dispersions along the $X-\Gamma-M-X$ path, colored by the phonon angular momentum L_z of each mode. (b,c) Real-space trajectories of atoms for the fourth and fifth phonon branches at Γ , showing circular atomic orbits with opposite senses of rotation on alternating sublattices, characteristic of chiral phonon polarization.

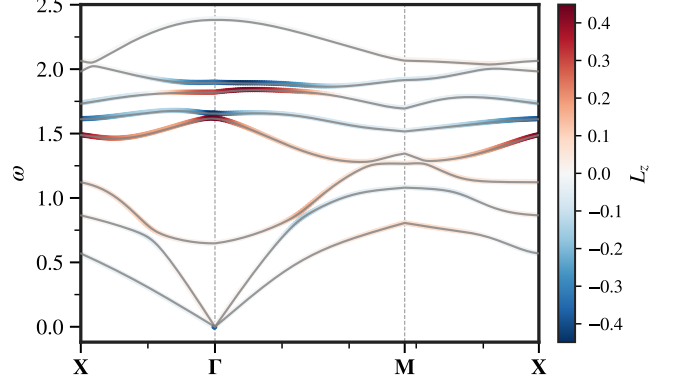


FIG. 15. Phonon band structure in the presence of a finite \mathcal{T} -breaking term $g = 0.1$ for a system with masses $(1.5, 1.0, 1.5, 1.0)$ and spring constants $K_1 = 1.0$, $K_2 = 0.5$, and $K_3 = 0.25$. The color scale represents the phonon angular momentum $L_z(\mathbf{k})$.

F. Infrared Circular Dichroism

Recently Fiorazzo *et al.* [48] presented a comprehensive microscopic theory of infrared magneto-optical effects arising from chiral phonons in solids, demonstrating that \mathcal{T} -breaking induces antisymmetric, frequency-dependent corrections to the dynamical matrix through the nuclear Berry curvature. While it is not the primary focus of our study, motivated by their work, we discuss in this section the results obtained by capturing the same physical mechanism within a minimal setting using the presented model. The details of the method are discussed in Appendix E. Unlike the full microscopic theory, the present implementation is phenomenological and neglects the frequency dependence of the nonadiabatic corrections and treats the \mathcal{T} -breaking coupling as a tunable parameter.

The \mathcal{T} -breaking term in the dynamical matrix gives certain optical phonons with finite angular momentum, leading to unequal coupling with left and right circularly polarized light. This results in an *infrared circular dichroism* (IR-CD), whose spectral response near a phonon resonance at frequency ω_0 takes the characteristic derivative-like form.

$$\Delta I(\omega) \simeq A \frac{(\Delta\omega)(\omega - \omega_0)}{(\omega - \omega_0)^2 + \gamma^2}, \quad (19)$$

where $\Delta\omega$ is the splitting of the chiral phonon doublet, γ is the linewidth, and $A \propto |\mathbf{p}_0|^2/\omega_0$ is proportional to the mode dipole strength. The amplitude of $\Delta I(\omega)$ grows linearly with both $\Delta\omega$ and the phonon pseudo-angular momentum, providing a direct optical signature of chiral phonons in the lattice.

In Fig. 16 we show the calculated IR-CD spectra for the square-octagon lattice with masses $(1, 2, 1, 2)$ and spring constants $K_1 = 1.0$, $K_2 = 0.5$, $K_3 = 0.25$. It

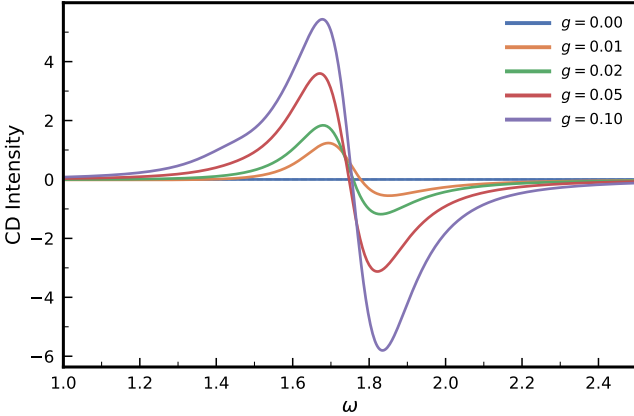


FIG. 16. Infrared circular dichroism (IR-CD) spectra of the square-octagon lattice for different time-reversal-symmetry-breaking strengths g . The calculations use masses $= (1, 2, 1, 2)$ and spring constants $K_1 = 1.0$, $K_2 = 0.5$, $K_3 = 0.25$. For $g = 0$, the dichroic response vanishes as expected from symmetry, while increasing g produces a derivative-shaped CD peak reflecting the growing splitting of the chiral phonon pair.

shows the characteristic derivative-like lineshape and for vanishing gyroscopic coupling ($g = 0$), the dichroic intensity is strictly zero, consistent with \mathcal{T} -symmetry and the absence of phonon angular momentum. As the \mathcal{T} -breaking parameter g increases, the CD amplitude grows approximately linearly. The sign reversal of $\Delta I(\omega)$ across the resonance corresponds to opposite absorption for the two photon helicities, providing a direct optical signature of chiral lattice dynamics.

In Fig. 17 we show the IR-CD spectra for different sublattice mass configurations at fixed coupling parameters $K_1 = 1.0$, $K_2 = 0.5$, $K_3 = 0.25$, and \mathcal{T} -breaking strength $g = 0.1$. Reversing the mass pattern between configurations such as $(1, 2, 1, 2)$ and $(2, 1, 2, 1)$ changes the relative amplitude and position of the peaks, indicating a possible redistribution of chiral oscillator strength among the modes. Increasing the sublattice masses systematically shifts the spectral features to lower frequencies, consistent with $\omega \propto \sqrt{K/M}$.

IV. SUMMARY AND CONCLUSION

In this work, we investigate the vibrational properties of the square-octagon lattice using a spring-mass model with variable interaction ranges and sublattice mass distributions. We construct the dynamical matrix allowing interactions up to 3rd-NN coupling. We show that in the absence of 3rd-NN coupling, the phonon spectrum exhibits frozen modes, whose dispersion and reorganization under weak NNN interactions lead to the opening of distinct frequency gaps. The inclusion of 3rd-NN couplings removes these frozen modes entirely, producing a

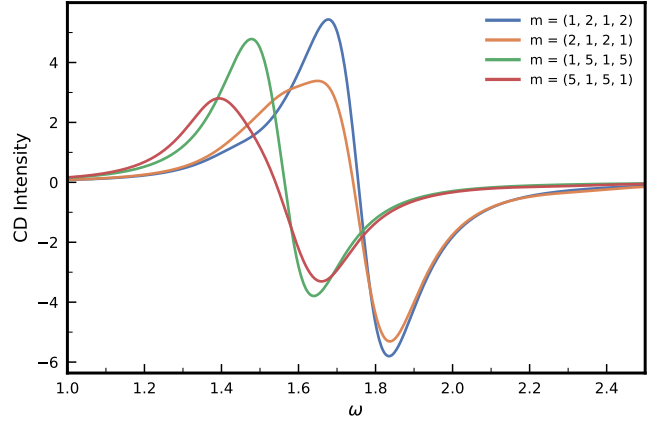


FIG. 17. Infrared circular dichroism spectra of the square-octagon lattice for different mass configurations at fixed $K_1 = 1.0$, $K_2 = 0.5$, and $K_3 = 0.25$ with $g = 0.1$.

smoother and more dispersive phonon landscape.

Systematic variations in the sublattice masses also reveal that mass contrast has significant influence on the phonon structure. Small asymmetries shift vibrational weight, modify frozen modes, and generate additional gaps, whereas large contrasts lead to mode localization, flat dispersive branches, and pronounced anisotropy. We further characterize the low-momentum response by analyzing both phase and group velocities, which exhibit clear fourfold anisotropy consistent with the underlying lattice symmetry. This anisotropy persists even in the long-wavelength limit, as verified by Fourier analysis of the velocity profiles, and evolves nonmonotonically with momentum. Iso-frequency contour analysis demonstrates how coupling strength, mass contrast, and sublattice configuration tune the degree of anisotropy, localization, and directional phonon transport.

Following the framework of Wang *et al.* [38], we further investigate the emergence of chiral phonons in the square-octagon lattice by introducing time reversal symmetry breaking. Motivated by the theoretical analysis of Fiorazzo *et al.* [48], we construct a simplified model to examine the corresponding infrared circular dichroism spectra, illustrating how chiral phonon modes couple selectively to circularly polarized light.

Our results show that the interplay of lattice geometry, long-range couplings, and sublattice mass asymmetry gives rise to a rich and tunable vibrational landscape featuring multiple phonon gaps, anisotropic transport, and mode localization. These findings can provide a framework for phonon band engineering in the square-octagon lattice systems and can be valuable for further studies on controlling thermal transport, designing phononic devices, and probing flat-band physics in mechanical systems. This work also extends the understanding of chiral phonons to a new lattice geometry and offers a foundation for exploring their broader physical consequences.

V. ACKNOWLEDGMENTS

R.K. would sincerely like to thank Subhajit Pramanick for his insightful discussions on the topic.

VI. CODE AND DATA AVAILABILITY

The relevant codes used to generate data for the current study are available at Zenodo [49].

Appendix A: Dynamical matrix

The explicit matrix entries of the dynamical matrix derived in Eqn. 15 are,

$$\begin{aligned}
 \mathbf{D}_{11} &= \frac{1}{m_A} [K_1(\mathbf{P}_1 + \mathbf{P}_2 + \mathbf{Y}) + K_2\mathbf{Y} + K_3\mathbf{Y}], \\
 \mathbf{D}_{22} &= \frac{1}{m_B} [K_1(\mathbf{P}_1 + \mathbf{P}_2 + \mathbf{X}) + K_2\mathbf{X} + K_3\mathbf{X}], \\
 \mathbf{D}_{33} &= \frac{1}{m_C} [K_1(\mathbf{P}_1 + \mathbf{P}_2 + \mathbf{Y}) + K_2\mathbf{Y} + K_3\mathbf{Y}], \\
 \mathbf{D}_{44} &= \frac{1}{m_D} [K_1(\mathbf{P}_1 + \mathbf{P}_2 + \mathbf{X}) + K_2\mathbf{X} + K_3\mathbf{X}], \\
 \mathbf{D}_{12} &= -\frac{K_1}{\sqrt{m_A m_B}} \mathbf{P}_1 e^{i\frac{(k_x - k_y)}{\sqrt{2}}} - \frac{K_3}{\sqrt{m_A m_B}} \mathbf{P}_1 e^{i\varphi_{12}^{(3)}}, \\
 \mathbf{D}_{14} &= -\frac{K_1}{\sqrt{m_A m_D}} \mathbf{P}_2 e^{-i\frac{(k_x + k_y)}{\sqrt{2}}} - \frac{K_3}{\sqrt{m_A m_D}} \mathbf{P}_2 e^{i\varphi_{14}^{(3)}}, \\
 \mathbf{D}_{23} &= -\frac{K_1}{\sqrt{m_B m_C}} \mathbf{P}_2 e^{-i\frac{(k_x + k_y)}{\sqrt{2}}} - \frac{K_3}{\sqrt{m_B m_C}} \mathbf{P}_2 e^{i\varphi_{23}^{(3)}}, \\
 \mathbf{D}_{34} &= -\frac{K_1}{\sqrt{m_C m_D}} \mathbf{P}_1 e^{-i\frac{(k_x - k_y)}{\sqrt{2}}} - \frac{K_3}{\sqrt{m_C m_D}} \mathbf{P}_1 e^{i\varphi_{34}^{(3)}}, \\
 \mathbf{D}_{13} &= -\frac{1}{\sqrt{m_A m_C}} [K_1 \mathbf{Y} e^{ik_y} + K_2 \mathbf{Y} e^{-i\sqrt{2}k_y} + K_3 \mathbf{Y} e^{i\varphi_{13}^{(3)}}] \\
 \mathbf{D}_{24} &= -\frac{1}{\sqrt{m_B m_D}} [K_1 \mathbf{X} e^{ik_x} + K_2 \mathbf{X} e^{-i\sqrt{2}k_x} + K_3 \mathbf{X} e^{i\varphi_{24}^{(3)}}]
 \end{aligned} \tag{A1}$$

where, $\varphi_{ij}^{(3)} = \mathbf{k} \cdot \Delta_{i \rightarrow j}^{(3)}$, and, $\Delta_{i \rightarrow j}^{(3)} = \mathbf{R}' + \tau_j - \tau_i$, $\mathbf{R}' = n_1 \mathbf{a}_1 + n_2 \mathbf{a}_2$ ($n_1, n_2 \in \mathbb{Z}$), where \mathbf{R}' is chosen so that $|\Delta_{i \rightarrow j}^{(3)}|$ equals the third-neighbour distance.

Appendix B: Phonon band structure in the absence of third neighbor coupling ($K_3 = 0$)

As a companion to the discussion in the text for the phonon bands for $K_3 \neq 0$, here we present the phonon spectra of the square-octagon lattice in the absence of 3rd-NN couplings ($K_3 = 0$). Figure 18(a-d) presents the phonon dispersions and DOS for a unit cell with equal atomic masses. A notable feature across all cases is the presence of two frozen modes, which produce sharp peaks in the DOS. For equal masses, these frozen modes occur

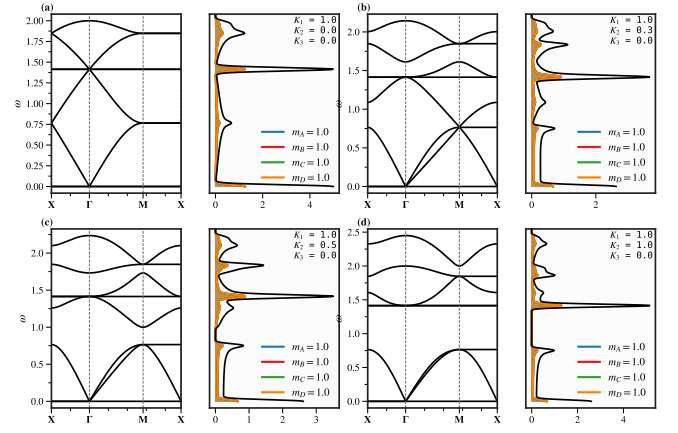


FIG. 18. Phonon dispersions along the $X-\Gamma-M-X$ path and the corresponding density of states for uniform masses and 3rd-NN coupling ($K_3 = 0$).

at $q = 0$ and $q = \sqrt{2}$. Introducing a weak NNN interaction (Fig. 18(b)) disperses some of these modes and broadens the DOS, signaling enhanced hybridization between localized and extended vibrations. With stronger NNN coupling (Fig. 18(c)), the band structure reorganizes and a gap opens. NN and NNN couplings become comparable (Fig. 18(d)), this gap widens further.

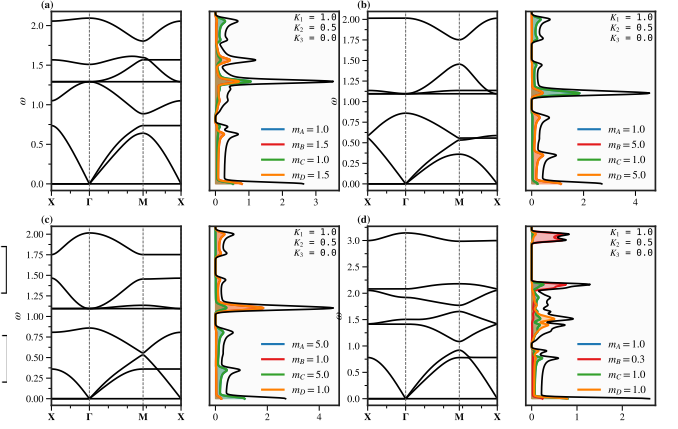


FIG. 19. Phonon dispersions along the $X-\Gamma-M-X$ path and the corresponding densities of states for the square-octagon lattice with $K_1 = 1.0$, $K_2 = 0.5$, and no 3rd-NN coupling ($K_3 = 0$). The sublattice masses are: (a) $m_A = m_C = 1.0$, $m_B = m_D = 1.5$, (b) $m_A = m_C = 1.0$, $m_B = m_D = 5.0$, (c) $m_A = m_C = 5.0$, $m_B = m_D = 1.0$, and (d) $m_A = m_C = m_D = 1.0$, $m_B = 0.3$.

Next, we allow the masses within the square-octagon unit cell to vary while keeping the 3rd-NN coupling zero and the NNN coupling moderate, as shown in Fig. 19. Compared to the uniform-mass case (Fig. 18), increasing a site mass shifts its vibrational weight to lower frequencies, consistent with $\omega = \sqrt{K/M}$, while large mass contrast enhances localization and produces sharper sublattice-resolved DOS peaks. For small mass

variations (Fig. 19(a)), the high-frequency bands shift downward, narrowing the gap observed in the uniform case. With stronger mass contrast (Fig. 19(c)), the high-frequency gap merges with the acoustic branches, though multiple phonon gaps persist. Introducing a very light atom to mimic a defect (Fig. 19(d)) opens a new gap just above the acoustic bands, with its contribution shifted to high frequencies.

Appendix C: Angular anisotropy: Derivation of a_4/a_0

To quantify the angular anisotropy of the phase velocity, we expand the function

$$v_p(\theta) = \frac{\omega(\mathbf{k})}{|\mathbf{k}|}, \quad \mathbf{k} = |k|(\cos \theta, \sin \theta),$$

in a Fourier series over the polar angle $\theta \in [0, 2\pi]$:

$$v_p(\theta) = A_0 + \sum_{n=1}^{\infty} [A_n \cos(n\theta) + B_n \sin(n\theta)], \quad (C1)$$

with coefficients

$$\begin{aligned} A_0 &= \frac{1}{2\pi} \int_0^{2\pi} v_p(\theta) d\theta, \\ A_n &= \frac{1}{\pi} \int_0^{2\pi} v_p(\theta) \cos(n\theta) d\theta, \\ B_n &= \frac{1}{\pi} \int_0^{2\pi} v_p(\theta) \sin(n\theta) d\theta. \end{aligned} \quad (C2)$$

The magnitude of the n -th Fourier component is

$$M_n = \sqrt{A_n^2 + B_n^2}. \quad (C3)$$

In particular, the zeroth coefficient A_0 represents the isotropic mean velocity, while M_4 quantifies the strength of the fourfold modulation. We therefore define the normalized anisotropy ratio

$$\frac{a_4}{a_0} = \frac{\sqrt{A_4^2 + B_4^2}}{A_0}. \quad (C4)$$

This dimensionless quantity measures the relative importance of the fourfold symmetry component compared to the isotropic average. For a perfectly isotropic dispersion one finds $a_4/a_0 = 0$, while finite values indicate fourfold anisotropy.

For numerical implementation, we evaluate $v_p(\theta)$ on a uniform grid of N angular points $\theta_j = 2\pi(j-1)/N$, $j = 1, \dots, N$, and compute the discrete Fourier transform

$$c_k = \frac{1}{N} \sum_{j=1}^N v_p(\theta_j) e^{-i(k-1)\theta_j}, \quad k = 1, \dots, N. \quad (C5)$$

These complex coefficients approximate the continuum Fourier series. The relations between c_k and the real

Fourier coefficients are

$$\begin{aligned} A_0 &\approx \text{Re}(c_1), \\ A_n &\approx 2 \text{Re}(c_{n+1}), \\ B_n &\approx -2 \text{Im}(c_{n+1}), \quad (n \geq 1). \end{aligned} \quad (C6)$$

Hence the fourfold amplitude is $M_4 \approx 2|c_5|$, and the anisotropy ratio is estimated as

$$\frac{a_4}{a_0} \approx \frac{2|c_5|}{\text{Re}(c_1)}. \quad (C7)$$

Appendix D: Iso-frequency plots in the absence of third neighbor coupling ($K_3 = 0$)

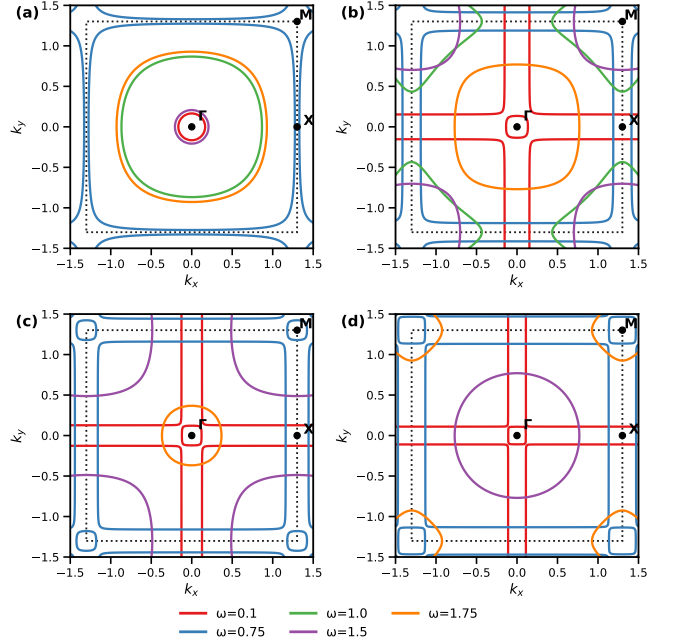


FIG. 20. Isofrequency contours of the square-octagon lattice with uniform masses ($m_\alpha = 1$), NN coupling $K_1 = 1.0$, no 3rd-NN coupling ($K_3 = 0$), and varying next-nearest-neighbor coupling K_2 . (a) $K_2 = 0$, contours are nearly circular at low ω . (b) $K_2 = 0.3$, weak NNN coupling introduces fourfold anisotropy. (c) $K_2 = 0.5$, stronger anisotropy produces visibly squared contours. (d) $K_2 = 1.0$, with NN and NNN couplings equal.

In Fig. 20 we show the isofrequency surfaces for the phonon bands discussed in Appendix B, evaluated for $K_3 = 0$ and equal atomic masses ($m_\alpha = 1$). For vanishing NNN coupling ($K_2 = 0$) (Fig. 20(a)), the isofrequency contours are nearly circular with only weak fourfold modulation. Introducing a weak NNN interaction ($K_2 = 0.3$) (Fig. 20(b)) produces square-shaped contours that reflect the underlying lattice symmetry and the onset of anisotropic group velocities. At stronger coupling, the phonon gaps identified earlier appear as missing frequency contours (Figs. 20(c,d)).

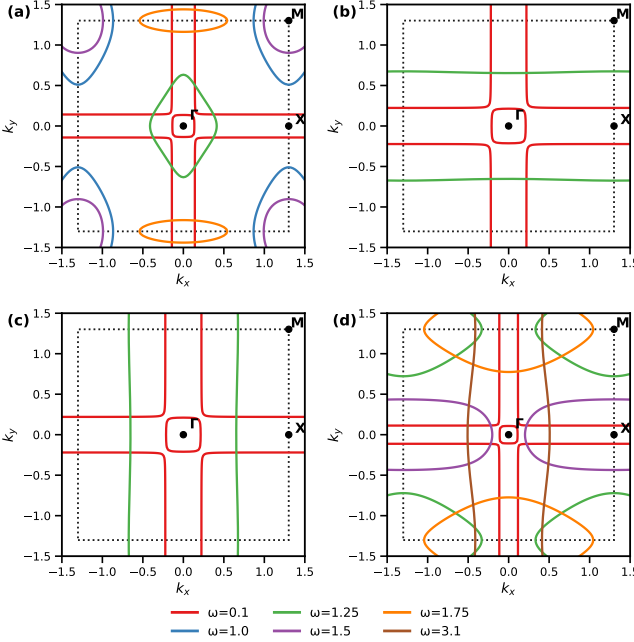


FIG. 21. Isofrequency contours of the square-octagon lattice with $K_1 = 1.0$, $K_2 = 0.5$, $K_3 = 0$, and varying sublattice masses. (a) $m_A = m_C = 1.0$, $m_B = m_D = 1.5$; (b) $m_A = m_C = 1.0$, $m_B = m_D = 5.0$; (c) $m_A = m_C = 5.0$, $m_B = m_D = 1.0$; (d) $m_A = m_C = m_D = 1.0$, $m_B = 0.3$.

We next fix the NN coupling at $K_1 = 1$ and a moderate NNN coupling at $K_2 = 0.5$, and vary the sublattice masses to examine how mass asymmetry influences the isofrequency contours. The results are shown in Fig. 21. For a small mass contrast ($m_A = m_C = 1.0$, $m_B = m_D = 1.5$) (Fig. 21(a)), the low-frequency anisotropy remains similar to the uniform-mass case, while the frozen mode near $\omega = 1.5$ appears as a rotated square. Assigning heavier atoms to the B and D sublattices (Fig. 21(b)) flattens the contours along k_x , forming nearly straight segments and suppressing group velocity along this direction. When the heavier atoms occupy the A and C sites (Fig. 21(c)), the anisotropy rotates by 90° , with the $\omega = 1.25$ contours flattening along k_y and reducing propagation in the y direction. Finally, introducing a very light atom ($m_A = m_C = m_D = 1.0$, $m_B = 0.3$) (Fig. 21(d)) produces anisotropic contours across multiple frequencies.

Appendix E: Infrared circular dichroism and analytical formulation

In the present study, \mathcal{T} -symmetry is broken through an antisymmetric gyroscopic term added to the real symmetric dynamical matrix:

$$D(\mathbf{k}) = D_0(\mathbf{k}) + ig G(\mathbf{k}), \quad (\text{E1})$$

where $D_0(\mathbf{k})$ represents the central-force contribution and $g G(\mathbf{k})$ encodes a velocity-dependent coupling of strength g . For a given phonon mode n , the angular momentum is defined as

$$L_z^{(n)} = \sum_{\alpha} m_{\alpha} \text{Im} \left[e_{\alpha x}^{(n)*} e_{\alpha y}^{(n)} \right], \quad (\text{E2})$$

where m_{α} is the atomic mass and $\mathbf{e}_{\alpha}^{(n)}$ is the normalized eigen-displacement of atom α . The angular momentum serves as a microscopic measure of lattice chirality and vanishes in the absence of \mathcal{T} -breaking ($g = 0$).

When light interacts with these chiral phonons, the coupling is governed by the mode-resolved electric dipole moment [48],

$$\mathbf{p}_n = \sum_s Z_s^* \cdot \mathbf{e}_s^{(n)}, \quad (\text{E3})$$

where Z_s^* denotes the Born effective charge tensor. The lattice contribution to the linear susceptibility tensor is then

$$\chi_{ij}(\omega) = \sum_n \frac{p_{n,i} p_{n,j}}{\omega_n^2 - \omega^2 - i\gamma_n \omega}, \quad (\text{E4})$$

with ω_n and γ_n the frequency and linewidth of the n -th phonon mode. In the circular polarization basis, $\mathbf{e}_{\pm} = (\hat{x} \pm i\hat{y})/\sqrt{2}$, the two helicity-resolved susceptibilities are

$$\chi_{\pm}(\omega) = \mathbf{e}_{\pm}^{\dagger} \chi(\omega) \mathbf{e}_{\pm} = \sum_n \frac{|\mathbf{e}_{\pm}^{\dagger} \mathbf{p}_n|^2}{\omega_n^2 - \omega^2 - i\gamma_n \omega}. \quad (\text{E5})$$

The absorption intensity for left- and right-circularly polarized light is proportional to

$$I_{\pm}(\omega) \propto \omega \text{Im} [\chi_{\pm}(\omega)], \quad (\text{E6})$$

and the resulting infrared circular dichroism signal is the difference between these two helicities,

$$\Delta I(\omega) = I_+(\omega) - I_-(\omega) \propto \omega \text{Im} [\chi_{xy}(\omega)]. \quad (\text{E7})$$

Near an isolated optical resonance, the two circular components experience slightly shifted phonon frequencies, $\omega_{0\pm} = \omega_0 \pm \Delta\omega/2$, due to \mathcal{T} -breaking. Expanding to first order in the splitting $\Delta\omega$, one obtains a simple analytic form for the dichroic response,

$$\Delta I(\omega) \simeq A \frac{(\Delta\omega)(\omega - \omega_0)}{(\omega - \omega_0)^2 + \gamma^2}, \quad (\text{E8})$$

where $A \propto |\mathbf{p}_0|^2/\omega_0$. This derivative-like lineshape, positive on one side of the resonance and negative on the other, reflects the opposite handedness of the two circularly polarized phonon modes. The amplitude of the dichroism scales linearly with the mode splitting $\Delta\omega$, which in turn is proportional to the \mathcal{T} -breaking strength g and the phonon angular momentum $L_z^{(n)}$. In the limit $g \rightarrow 0$, both $L_z^{(n)}$ and $\Delta I(\omega)$ vanish, confirming that IR-CD originates purely from the lattice's chiral dynamics.

-
- [1] I. Tamm, Über die quantentheorie der molekularen lichtzerstreuung in festen körpern, *Zeitschrift für Physik* **60**, 345 (1930).
- [2] L. Zhang and Q. Niu, Chiral phonons at high-symmetry points in monolayer hexagonal lattices, *Phys. Rev. Lett.* **115**, 115502 (2015).
- [3] H. Zhu, J. Yi, M.-Y. Li, J. Xiao, L. Zhang, C.-W. Yang, R. A. Kaindl, L.-J. Li, Y. Wang, and X. Zhang, Observation of chiral phonons, *Science* **359**, 579 (2018).
- [4] H. Ueda, M. García-Fernández, S. Agrestini, C. P. Romao, J. van den Brink, N. A. Spaldin, K.-J. Zhou, and U. Staub, Chiral phonons in quartz probed by x-rays, *Nature* **618**, 946 (2023).
- [5] M. Pols, G. Brocks, S. Calero, and S. Tao, Chiral phonons in 2d halide perovskites, *Nano Letters* (2025).
- [6] J. Luo, T. Lin, J. Zhang, X. Chen, E. R. Blackert, R. Xu, B. I. Yakobson, and H. Zhu, Large effective magnetic fields from chiral phonons in rare-earth halides, *Science* **382**, 698 (2023).
- [7] R. Sasaki, Y. Nii, and Y. Onose, Magnetization control by angular momentum transfer from surface acoustic wave to ferromagnetic spin moments, *Nature communications* **12**, 2599 (2021).
- [8] K. Kim, E. Vetter, L. Yan, C. Yang, Z. Wang, R. Sun, Y. Yang, A. H. Comstock, X. Li, J. Zhou, *et al.*, Chiral-phonon-activated spin seebeck effect, *Nature Materials* **22**, 322 (2023).
- [9] T. Saito, K. Misaki, H. Ishizuka, and N. Nagaosa, Berry phase of phonons and thermal hall effect in nonmagnetic insulators, *Phys. Rev. Lett.* **123**, 255901 (2019).
- [10] T. Qin, J. Zhou, and J. Shi, Berry curvature and the phonon hall effect, *Phys. Rev. B* **86**, 104305 (2012).
- [11] T. Zhang, S. Murakami, and H. Miao, Weyl phonons: the connection of topology and chirality, *nature communications* **16**, 3560 (2025).
- [12] T. Zhang, Z. Huang, Z. Pan, L. Du, G. Zhang, and S. Murakami, Weyl phonons in chiral crystals, *Nano Letters* **23**, 7561 (2023).
- [13] P. V. Sreenivasa Reddy and G.-Y. Guo, Coexistent topological and chiral phonons in chiral RhGe: An ab initio study, *Phys. Rev. B* **112**, 155126 (2025).
- [14] S. Mishra, A. Chakraborty, D. S. Galvao, P. A. Autreto, and A. K. Singh, Chiral phonons in graphyne, *arXiv preprint arXiv:2508.11040* (2025).
- [15] K. Ishito, H. Mao, Y. Kousaka, Y. Togawa, S. Iwasaki, T. Zhang, S. Murakami, J.-i. Kishine, and T. Satoh, Truly chiral phonons in α -hgs, *Nature Physics* **19**, 35 (2023).
- [16] K. Ohe, H. Shishido, M. Kato, S. Utsumi, H. Matsuura, and Y. Togawa, Chirality-induced selectivity of phonon angular momenta in chiral quartz crystals, *Phys. Rev. Lett.* **132**, 056302 (2024).
- [17] S. D. Huber, Topological mechanics, *Nature Physics* **12**, 621 (2016).
- [18] Y.-H. Liu, C. C. Chang, R.-L. Chern, and C. C. Chang, Phononic band gaps of elastic periodic structures: A homogenization theory study, *Phys. Rev. B* **75**, 054104 (2007).
- [19] C. Croënne, E. Lee, H. Hu, and J. Page, Band gaps in phononic crystals: Generation mechanisms and interaction effects, *AIP Advances* **1** (2011).
- [20] G. Gantzounis, N. Papanikolaou, and N. Stefanou, Multiple-scattering calculations for layered phononic structures of nonspherical particles, *Phys. Rev. B* **83**, 214301 (2011).
- [21] M. B. Muhlestein, Effective acoustic metamaterial homogenization based on hamilton's principle with a multiple scales approximation, *The Journal of the Acoustical Society of America* **147**, 3584 (2020).
- [22] M. Yang, G. Ma, Y. Wu, Z. Yang, and P. Sheng, Homogenization scheme for acoustic metamaterials, *Phys. Rev. B* **89**, 064309 (2014).
- [23] S. Nikitenkova and A. Potapov, Dispersion properties of two-dimensional phonon crystals with a hexagonal structure, *Acoustical Physics* **56**, 909 (2010).
- [24] M. S. Kushwaha, P. Halevi, L. Dobrzynski, and B. Djafari-Rouhani, Acoustic band structure of periodic elastic composites, *Phys. Rev. Lett.* **71**, 2022 (1993).
- [25] Y. Tanaka, Y. Tomoyasu, and S.-i. Tamura, Band structure of acoustic waves in phononic lattices: Two-dimensional composites with large acoustic mismatch, *Phys. Rev. B* **62**, 7387 (2000).
- [26] J. Mei, Z. Liu, and C. Qiu, Multiple-scattering theory for out-of-plane propagation of elastic waves in two-dimensional phononic crystals, *Journal of Physics: Condensed Matter* **17**, 3735 (2005).
- [27] J. O. Vasseur, P. A. Deymier, B. Chenni, B. Djafari-Rouhani, L. Dobrzynski, and D. Prevost, Experimental and theoretical evidence for the existence of absolute acoustic band gaps in two-dimensional solid phononic crystals, *Phys. Rev. Lett.* **86**, 3012 (2001).
- [28] S. Yang, J. H. Page, Z. Liu, M. L. Cowan, C. T. Chan, and P. Sheng, Focusing of sound in a 3D phononic crystal, *Phys. Rev. Lett.* **93**, 024301 (2004).
- [29] M. Wilm, A. Khelif, S. Ballandras, V. Laude, and B. Djafari-Rouhani, Out-of-plane propagation of elastic waves in two-dimensional phononic band-gap materials, *Phys. Rev. E* **67**, 065602 (2003).
- [30] Z. Liu, X. Zhang, Y. Mao, Y. Y. Zhu, Z. Yang, C. T. Chan, and P. Sheng, Locally resonant sonic materials, *science* **289**, 1734 (2000).
- [31] M. Sigalas and N. Garcia, Theoretical study of three dimensional elastic band gaps with the finite-difference time-domain method, *Journal of Applied Physics* **87**, 3122 (2000).
- [32] P. Lambin, A. Khelif, J. O. Vasseur, L. Dobrzynski, and B. Djafari-Rouhani, Stopping of acoustic waves by sonic polymer-fluid composites, *Phys. Rev. E* **63**, 066605 (2001).
- [33] M. Kafesaki and E. N. Economou, Multiple-scattering theory for three-dimensional periodic acoustic composites, *Phys. Rev. B* **60**, 11993 (1999).
- [34] C. L. Kane and T. C. Lubensky, Topological boundary modes in isostatic lattices, *Nature Physics* **10**, 39 (2014).
- [35] E. Prodan and C. Prodan, Topological phonon modes and their role in dynamic instability of microtubules, *Phys. Rev. Lett.* **103**, 248101 (2009).
- [36] N. Berg, K. Joel, M. Koolek, and E. Prodan, Topological phonon modes in filamentary structures, *Phys. Rev. E* **83**, 021913 (2011).
- [37] R. Süsstrunk and S. D. Huber, Classification of topological phonons in linear mechanical metamaterials, *Pro-*

- ceedings of the National Academy of Sciences **113**, E4767 (2016).
- [38] Q. Wang, S. Li, J. Zhu, H. Chen, W. Wu, W. Gao, L. Zhang, and S. A. Yang, Chiral phonons in lattices with C_4 symmetry, *Phys. Rev. B* **105**, 104301 (2022).
- [39] H. Chen, W. Wu, S. A. Yang, X. Li, and L. Zhang, Chiral phonons in kagome lattices, *Phys. Rev. B* **100**, 094303 (2019).
- [40] X. Xu, W. Zhang, J. Wang, and L. Zhang, Topological chiral phonons in center-stacked bilayer triangle lattices, *Journal of Physics: Condensed Matter* **30**, 225401 (2018).
- [41] B. Pal, Nontrivial topological flat bands in a diamond-octagon lattice geometry, *Phys. Rev. B* **98**, 245116 (2018).
- [42] D. O. Oriekhov, V. P. Gusynin, and V. M. Loktev, Orbital susceptibility of t-graphene: Interplay of high-order van hove singularities and dirac cones, *Phys. Rev. B* **103**, 195104 (2021).
- [43] S. Zhang, Z. Huang, M. Du, T. Ying, L. Du, and T. Zhang, The chirality of phonons: Definitions, symmetry constraints, and experimental observation, *arXiv preprint arXiv:2503.22794* (2025).
- [44] L. Zhang, J. Ren, J.-S. Wang, and B. Li, Topological nature of the phonon hall effect, *Phys. Rev. Lett.* **105**, 225901 (2010).
- [45] A. Holz, Phonons in a strong static magnetic field, *Il Nuovo Cimento B (1971-1996)* **9**, 83 (1972).
- [46] T. Kariyado and Y. Hatsugai, Manipulation of dirac cones in mechanical graphene, *Scientific reports* **5**, 18107 (2015).
- [47] L. Zhang and Q. Niu, Angular momentum of phonons and the einstein-de haas effect, *Phys. Rev. Lett.* **112**, 085503 (2014).
- [48] C. Fiorazzo, C.-H. Park, I. Souza, and M. Calandra, Theory of infrared magneto-optical effects from chiral phonons in solids, *Phys. Rev. B* **112**, 094307 (2025).
- [49] R. Kiran, *Phonon dynamics and chiral modes in the two-dimensional square-octagon lattice : Code for the paper*, Zenodo (2025).